

# A simulation method to estimate task-specific uncertainty in 3D Microscopy

Giovanni Moroni<sup>1,2</sup>, Wahyudin P. Syam<sup>3</sup>, and Stefano Petrò<sup>2</sup>

<sup>1</sup> School of Mechanical Engineering, Tongji University, Cao An Road, 201804 Shanghai, P.R. of China

<sup>2</sup> Mechanical Engineering Department, Politecnico di Milano, Via La Masa 1, 20156 Milan, Italy

<sup>3</sup> Manufacturing Metrology Team, Faculty of Engineering, University of Nottingham, NG7 2RD, Nottingham, UK

Corresponding author: Wahyudin P. Syam ([Wahyudin.syam@nottingham.ac.uk](mailto:Wahyudin.syam@nottingham.ac.uk))

## Abstract:

Traceability in micro-metrology requires an infrastructure of accredited metrology institutes, effective performance verification procedures, and task specific uncertainty estimation. Focusing on the latter, this paper proposes an approach for the task specific uncertainty estimation based on simulation for a generic 3D microscope. The proposed simulation approach is based on the identification and a successive parameter estimation of an empirical model of measured points. The model simulates the probing error of the 3D microscope based on a Gaussian process model, thus including the correlation among close points. Parameters for the error simulation are estimated by a deep analysis of error sources of the 3D microscope. Validations of the proposed simulation approach are carried out in the case of focus variation microscopy (FVM), considering several case studies. The procedure proposed in the ISO/TS 15530-4 standard are applied for validation.

Keywords: Uncertainty, 3D microscopy, geometrical metrology, micro-metrology, ISO/TS 15530-4, focus-variation.

## 1. Introduction

Micro-engineered components are important since they can integrate functions and intelligence into products [1]. These products need micro-geometrical metrology to verify their compliance to tolerances. Coordinate measuring systems (CMSs), being suitable for micro-geometrical metrology are in most cases non-contact (optical) instruments, due to their flexibility in accessing the surface of parts, elimination of the risk of damaging small and delicate micro features and fast data acquisition rate [2]. Among the others, 3D microscopy (3DM) seems very promising and already counts a lot of industrial applications, particularly in the field of surface analysis. 3DM gathers technique like coherence scanning interferometry, phase shifting interferometry, confocal scanning microscopy, confocal chromatic microscopy, digital holography, and focus variation microscopy. Most 3DM techniques are based on the sequential acquisition of images of the sample, while changing the distance between the sample and the objective lens.

### 1.1 Measurement traceability and uncertainty

Regardless of the considered measuring instruments, traceability of measurements is very important for a reliable measurement result in the case of micro-geometrical metrology as well. Traceability requires not only periodical instrument performance verification to check if measuring instruments behave as stated by their manufacturer

49 or according to some predefined performance indexes, but also measurement  
50 uncertainty must be stated to guarantee measurement comparability [3]. The subject of  
51 performance verification has been addressed by the authors in previous papers [4, 5]:  
52 this paper addresses the problem of the uncertainty estimation.

53 The main reference for measurement uncertainty estimation is the “Guide to the  
54 expression of uncertainty in measurement” (GUM) [6]. According to the GUM, when  
55 a final measurement result comes from several distinct measurement data processes,  
56 the uncertainty is derived based on the propagation of the uncertainty from each  
57 uncertainty contributor along the data processing chain, thus GUM requires a closed  
58 form mathematical model of the measurement. In addition, for coordinate metrology,  
59 measurement uncertainty is “task-specific” [7], i.e. a single measuring instrument can  
60 perform several different measurement tasks with different measuring strategies, which  
61 are characterized by a different uncertainty [8]; hence the GUM method is difficult to  
62 apply.

63 The ISO 15530-3 [9] and ISO/TS 15530-4 [10] standards propose alternative methods  
64 to effectively estimate the measurement uncertainty for coordinate metrology. The ISO  
65 15530-3 method needs expensive calibrated artifacts; hence it is not suitable when a  
66 product has many variants, as it would require many different calibrated artifacts, or  
67 when small production volume cannot justify the cost of a calibrated artifact. The  
68 ISO/TS 15530-4 simulation method seems more promising in the case of high product  
69 or high demand variability. The main drawback of the simulation method is its  
70 computational intensity [11], but the continuous reduction of computational costs  
71 should reduce this issue.

72

### 73 *1.2 Simulation approaches*

74 A simulation-based approach seems to be the most promising solution to estimate a  
75 task-specific measurement uncertainty, especially for optical-distance sensor  
76 instruments, as suggested by Evans [11] in the case of interferometry. Baldwin et al.  
77 [9] used a simulation approach to estimate the uncertainty in tactile-CMM  
78 measurement. They simulated CMM geometric errors and incorporated them in the  
79 kinematic model of the CMM, so that the nominal position of points could be modified.  
80 Kruth et al. [12] proposed a similar approach, with addition of part form deviation as  
81 an uncertainty source. Cheung et al. [13] also used a similar approach to estimate the  
82 uncertainty in the case of free-form surface measurements. All these simulation  
83 approaches neglect the presence of spatial correlations among the sampled points.

84 In general, a simulation approach relies on a point perturbation process (an error  
85 simulator) generating a perturbation of a reference cloud of points, as shown in Figure  
86 1. Detailed explanation of the framework applied to CMMs was described by Trapet  
87 and Waldele [14]. The scheme consists of two paths, the first one (Figure 1: black  
88 arrow) estimates a measurement result  $Y$ , while the second one (Figure 1: red arrow)  
89 estimates the measurement uncertainty  $U$ . The first path is explained as follows: a point  
90 cloud is obtained by the selected measuring system using a defined measuring strategy.  
91 This point cloud is then processed to calculate the measurement result  $Y$ . The second  
92 path starts from the same sampled point cloud. A point perturbation process by  
93 measurement error simulation is applied to the original point cloud. The perturbed point  
94 cloud is processed by the same numerical algorithm that is gathered to the measurement  
95 result and the results are stored. The simulation of the error is repeated for an adequate  
96 number of times (usually a few thousand) and the simulated measurement results are  
97 stored. The estimated uncertainty  $u_{sim}$  ( $U = 2 u_{sim}$ ) of a measurement is the sample  
98 standard deviation of the stored results from the simulation runs.

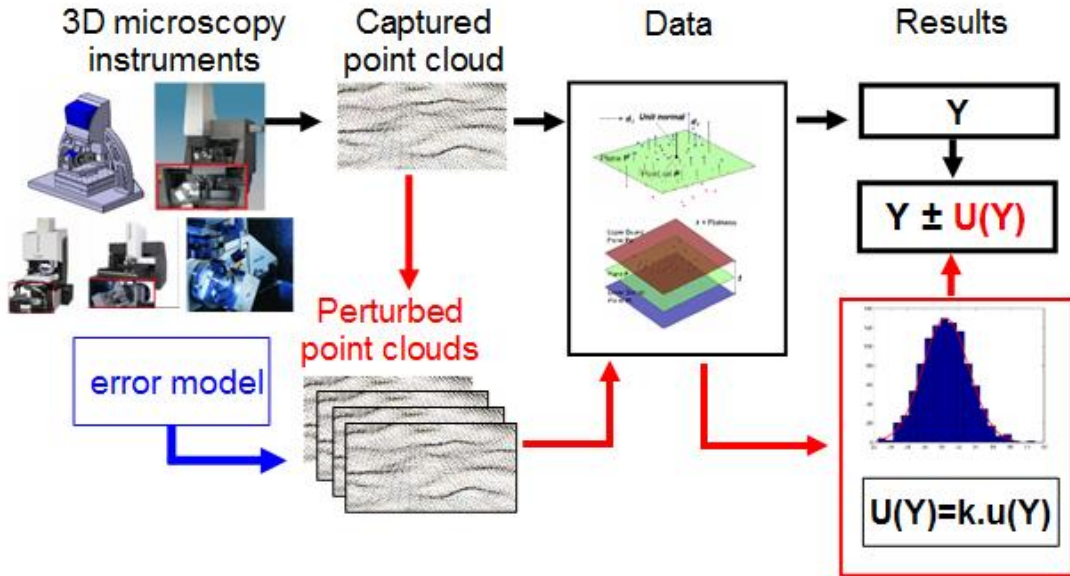


Figure 1: Framework a simulation method for the uncertainty estimate.

### 1.3 Research aim

In this paper, a simulation-based approach considering spatial correlation among points is proposed. The proposed model does not directly take into consideration physical phenomena related to interactions between materials and light; rather the model includes the effect of the physical interaction between the materials and the light inside several uncertainty sources, e.g. material types, and parameters of the simulation.

There are several technical reasons behind this consideration. First, even if well-established physical models exist for the interaction between electromagnetic waves and matter, their application is numerically impractical to apply and to the degree of accuracy required for 3DM measurement simulation. In general, the intensity value on each single pixel is not completely independent of the others. Hence, a single ray coming to the complementary metal-oxide semiconductor (CMOS) sensor has some degree of correlation with its neighbor ray of light [15]. And finally, some techniques add an additional contribution to the correlation among points, as the optimization function allowing the identification of the coordinates of the single point is calculated considering the neighboring pixels, selected by a windowing process [15].

Hence, to empirically model this phenomenon, the basis of the methodology is a Gaussian process [16], in which data are randomly distributed according to a multivariate Gaussian distribution, whose covariance structure depends on the spatial distribution of points. The multivariate Gaussian process can capture and simulate the correlation among points.

This paper is structured as follows. Section 2 describes the mathematical model allowing the simulation of the correlated points. Section 3 introduces Focus Variation Microscopy (FVM) as technology considered for the validation of the approach, and then focuses on the estimation of the parameters required to run the simulation. Finally, section 4 validates both the model and the estimation of the parameters according to the ISO/TS 15530-4 standard.

## 2. Task-specific uncertainty estimation by simulation in 3DM

The proposed approach relies on a point perturbation process (an error simulator) adopting a Gaussian process model taking into account the correlation among points,

132 as shown in Figure 1. A correlation means that the error behavior of a point depends on  
 133 other points within a certain distance from it. The simulation approach (figure 1, blue  
 134 box) uses a Gaussian process model completely defined by a variogram function, we  
 135 call it “variogram error model”. The need of this kind of model arises from how a 3DM  
 136 measurement is taken. As explained in section 1.3, it is expected that the measurement  
 137 errors of the single sampling points are not independent but correlated. An independent  
 138 simulation of them could then lead to a simulation far from the reality. The use of a  
 139 Gaussian process described by a variogram error model allows the simulation of non-  
 140 independent measurement errors, coherently with the measurement method.

### 143 2.1 Mathematical model for the simulation of a perturbed cloud of points

144 The core of the uncertainty estimation by simulation is the model for the perturbation  
 145 of the point cloud. In general, the perturbation of the cloud of points is given  
 146  $\varepsilon_{\theta_x}$ ,  $\varepsilon_{\theta_y}$ ,  $\varepsilon_{\theta_z}$ , which are rotation errors with respect to  $x$ ,  $y$  and  $z$  axes, and  $\varepsilon_x$ ,  $\varepsilon_y$ ,  $\varepsilon_z$  i.e.  
 147 linear errors along  $x$ ,  $y$  and  $z$  directions, respectively. Once these perturbations have  
 148 been generated for each point,  $\mathbf{p}_i'$ , the coordinates of a single perturbed point, can be  
 149 generated from the original measured points  $\mathbf{p}_i$ , (both are expressed in homogeneous  
 150 coordinates) by multiplying the measured points  $\mathbf{p}_i$  time an error matrix,  $\mathbf{T}_{err}$ , that is:

$$152 \quad \mathbf{p}_i' = \mathbf{T}_{err} \mathbf{p}_i = \begin{bmatrix} 1 & -\varepsilon_{\theta_z} & \varepsilon_{\theta_y} & \varepsilon_x \\ \varepsilon_{\theta_z} & 1 & -\varepsilon_{\theta_x} & \varepsilon_y \\ -\varepsilon_{\theta_y} & \varepsilon_{\theta_x} & 1 & \varepsilon_z \\ 0 & 0 & 0 & 1 \end{bmatrix} \mathbf{p}_i \quad (1)$$

153 In 3DM most of the error terms can be neglected. In fact, the  $x$  and  $y$  coordinates are  
 154 not directly measured, but considered at their nominal value, as defined by the objective  
 155 lens magnification and the image sensor size of the 3DM. Moreover, during the scan  
 156 the  $x$  and  $y$  do not move, and the translation along  $z$  is very small, so rotation errors are  
 157 negligible. As such, the model can be simplified considering only the  $\varepsilon_z$  term.

159 A correlated error for the  $i$ -th point,  $\varepsilon_{z_i}$ , is generated by sampling from a multi-variate  
 160 Gaussian distribution. The multivariate normal distribution density function is  
 161 formulated as:

$$163 \quad f(\mathbf{p}, \boldsymbol{\mu}, \boldsymbol{\Sigma}) = \frac{1}{\sqrt{|\boldsymbol{\Sigma}|} (2\pi)^m} e^{-\frac{1}{2}(\mathbf{p}-\boldsymbol{\mu})\boldsymbol{\Sigma}^{-1}(\mathbf{p}-\boldsymbol{\mu})} \quad (2)$$

164 where  $m$  is the dimension of the multivariate, i.e. the number of points,  $\mathbf{p}$  represents the  
 165 random vector with mean  $\boldsymbol{\mu}$  and  $\boldsymbol{\Sigma}$  is a  $m \times m$  variance-covariance matrix which  
 166 represents correlation. As the cloud of points is being randomly perturbed, the  $\boldsymbol{\mu}$  term  
 167 is set equal to 0. There are several ways of modelling  $\boldsymbol{\Sigma}$ . Among the others, we have  
 168 selected the use of the variogram  $2\gamma(\bullet)$  [16]. The variogram is well known and widely  
 169 applied in spatial statistics, as its estimation is more robust compared to its competitor  
 170 method. The variogram function, together with the mean vector  $\boldsymbol{\mu}$ , fully characterizes  
 171 the Gaussian process. Here we will address only isotropic homogeneous variogram  
 172 function, as they are the simplest type of variograms, to simplify the discussion.  
 173 Moreover, they have been found to be adequate for our case study. Details on non-  
 174 isotropic homogeneous variograms can be found in the proposed literature. An isotropic  
 175 homogeneous variogram function is defined as:

176  $2\gamma(\mathbf{x}_1, \mathbf{x}_2) = 2\gamma(h) = E[(Z(\mathbf{x}_1) - Z(\mathbf{x}_2))^2]$  (3)

177

178 where  $2\gamma(\bullet)$  is the variogram function,  $h$  is the lag (distance) between the generic

179 locations  $\mathbf{x}_1$  and  $\mathbf{x}_2$ , and  $Z(\mathbf{x})$  is a response function at  $\mathbf{x}$  (in 3DM the  $z$ -coordinate of a

180 point). Please note that the assumption  $2\gamma(\mathbf{x}_1, \mathbf{x}_2) = 2\gamma(h)$  implies the variogram is isotropic.

181 The typical shape of a  $\gamma(\bullet)$  function is illustrated in Figure 2. Example functions suitable

182 to model isotropic homogeneous variogram models, but many more exist in literature,

183 are:

184

$$\gamma(h) = \begin{cases} 0 & h = 0 \\ n + s \left( 1 - \exp\left(-3\frac{h^2}{r^2}\right) \right) & h \neq 0 \end{cases} \text{ Gaussian model}$$

185

$$\gamma(h) = \begin{cases} 0 & h = 0 \\ n + s \left( 1 - \exp\left(-3\frac{h}{r}\right) \right) & h \neq 0 \end{cases} \text{ Exponential model} \quad (4)$$

$$\gamma(h) = \begin{cases} 0 & h = 0 \\ n + s \left( 1 - \exp\left(-3\frac{h}{r}\right) \right) & 0 < h \leq r \\ n + s & h \geq r \end{cases} \text{ Spherical model}$$

186

187 where  $s$ ,  $n$ ,  $r$  are a sill, nugget, and range, respectively. These three parameters

188 characterize all variogram models (Figure 2). Nugget ( $n$ ) is a non-zero limit

189 representing a discontinuity in a variogram origin. The nugget represents the pure white

190 noise included in the random error. Sill ( $s$ ) quantifies the error dispersion at infinite

191 distance, i.e. global correlated and uncorrelated measurement noise. Range ( $r$ ) is a

192 measure of the distance up to which the measurement noise is significantly correlated.

193 Supposing the variogram error model and its parameters are known, having defined

194 a set of locations  $\mathbf{x}$ , the  $\Sigma$  matrix can be built as

195

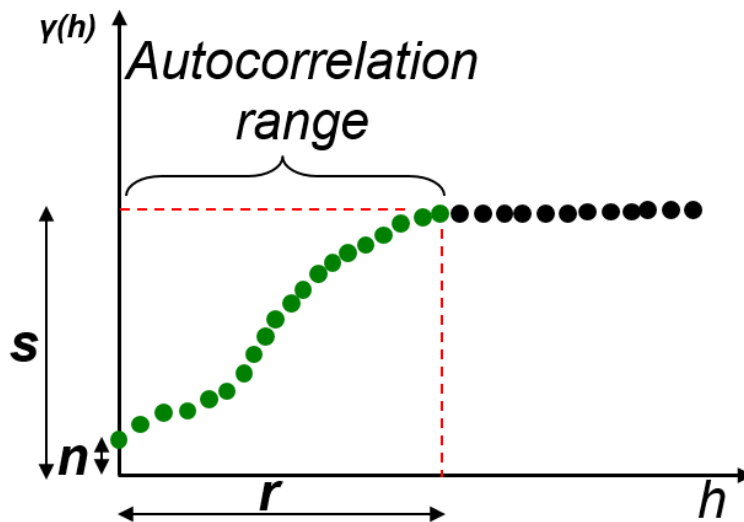
196  $\Sigma_{ij} = s - \gamma(\mathbf{x}_i, \mathbf{x}_j)$  (5)

197

198 Once the  $\Sigma$  matrix is known any multi-normal random number generator can be applied

199 to generate the  $\varepsilon_{zi}$  term at the  $\mathbf{x}_i$  location.

200



201

202

203

Figure 2: Illustration of variogram function and its  $s$ ,  $r$ ,  $n$  parameters.

## 204 2.2 Estimation of the variogram parameters for the simulation

205 The variogram model and its parameters need experimental identifications and  
206 evaluations. From experimental data, a least-square method is usually adopted to fit the  
207 empirical model of the variogram. Given a set of observations  $Z(\mathbf{x}_i)$  (e.g. a single scan  
208 of a surface by 3DM), the value of the variogram at distance  $h$  can be estimated as  
209

$$210 \hat{\gamma}(h) = \frac{1}{2|N(h)|} \sum_{N(h)} (Z(\mathbf{x}_i) - Z(\mathbf{x}_j))^2 \quad (6)$$

$$211 N(h) = \{(\mathbf{x}_i, \mathbf{x}_j) \mid \|\mathbf{x}_i - \mathbf{x}_j\| = h\} \quad (7)$$

212

213 In the specific case of 3DM, as the points are locate on an evenly spaced grid, the  
214 possible values of  $h$  are well defined, so there are a series of well-defined values of  
215  $\hat{\gamma}(h)$ . The  $\hat{\gamma}(h)$  are then fitted, considering different variogram models. Based on  $R^2$   
216 of the least-square fitting, the best-fitted variogram model is selected, and then, the  $n$ ,  
217  $s$ , and  $r$  parameters are estimated.

218 The least square estimation of the  $s$ ,  $n$ , and  $r$  parameters is in general applicable to a  
219 single sampled surface. It is then evident that the resulting parameters will be specific  
220 for the particular condition at which the scan has been conducted, e.g. material type. To  
221 have parameters that can be applied in a larger variety of conditions, we must modify  
222 them in order to take into account other uncertainty contributors. While the estimate of  
223 the nugget and the range can be properly estimated on a single scan, the sill, being  
224 representative of the overall variability of the measurement noise (correlated and  
225 uncorrelated), should include all the uncertainty contributors, and not only those from  
226 the condition at which it has been characterized so far. Hence, the parameter  $s$  resulting  
227 from the least square fitting shall be combined with other error sources before the  
228 simulation, according to the formula:

229

$$230 s_{sim} = \sqrt{s^2 + \sum s_i^2} \quad (8)$$

231

232 where  $s$  is the sill originally obtained from the fitted model of the variogram and  $s_i$   
233 is the contribution related with the  $i^{th}$  source of error. The estimate of the  $s_i$  terms  
234 require a deep analysis of the specific uncertainty sources affecting a particular 3D  
235 microscope, and an extensive experimental investigation of them. Once the  
236 contributors are known, their value can be extended to any future measurement.  
237

## 238 3. Case study: the uncertainty estimation for a Focus Variation Microscope

239

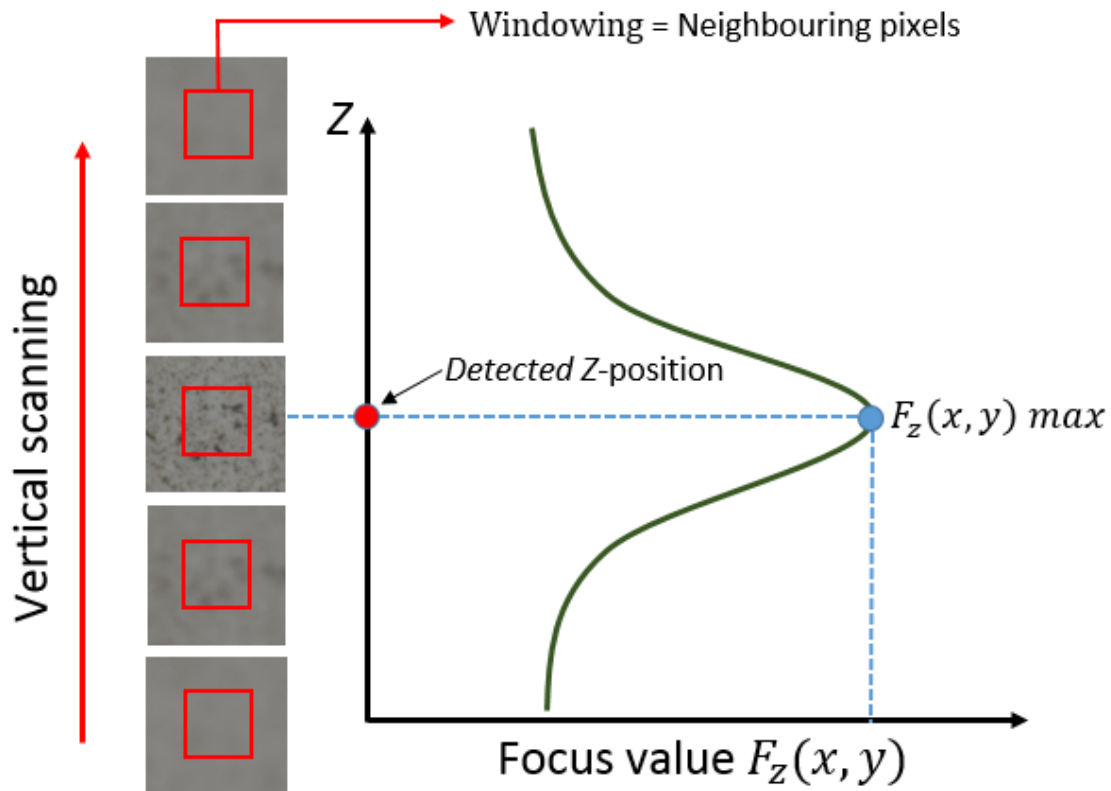
240 Focus variation microscopy (FVM) is considered in this study as an example of 3DM.  
241 The FVM instrument used to demonstrate the proposed simulation approach is a 4<sup>th</sup>  
242 generation FVM instrument by Alicona Imaging GmbH.

243 A FVM works based on the local focus condition of a stack of images taken at  
244 different distances from the measured surface to the FVM objective lens. The FVM  
245 working principle is as follows (see Figure 3): first, a stack of images is taken over a  
246 specified range of  $z$ -level (the distance from the measured surface to the scanning  
247 objective lens); the stack image acquisition is usually obtained by mechanically moving  
248 the objective lens of the FVM. For each  $z$ -level and for each pixel of the related stacked  
249 images, a focus value  $F_z(x, y)$ , which is a contrast of a pixel with respect to its  
250 neighboring pixels, is calculated. In most cases, the more the image is in focus, the

251 higher the focus value is. For each pixel a mathematical fitting procedure is applied to  
 252 the calculated focus values at each level, and the detected  $z$ -coordinate of a point is  
 253 determined corresponding to the  $z$ -level with the highest  $F_z(x, y)$  [15].

254 One fundamental advantage of a FVM instrument compared to other optical  
 255 microscopy is its large working volume and its long working distance of the objective  
 256 lens. This fundamental advantage provides the possibility of measuring the geometrical  
 257 properties of a part.

258 The FV values calculated for each  $(i, j)$  pixel locations are obtained by comparing its  
 259 contrast with respect to the intensity of its neighbor pixels.  
 260



261  
 262 Figure 3: FVM working principle by calculating a focus value inside a windowing  
 263 area.  
 264

### 265 3.1. Estimation of the variogram parameters

266 Different materials can be characterized by different variograms. In this study, we  
 267 consider calibrated plates of aluminum (Al), stainless steel (SS), and titanium (Ti) for  
 268 the variogram characterizations. It is worth to note that the variogram characterization  
 269 data need to be obtained from a real surface in order to take into account the physical  
 270 properties of the real measured surface, e.g. a roughness effect, local slope effect,  
 271 reflectance effect, measurement angle effect and speckle noise effect of the surface to  
 272 be included into the simulation process. Hence the variogram model takes into account  
 273 the material type as uncertainty source. The variogram data from the actual surface  
 274 measurements from the mentioned three materials will be used for uncertainty  
 275 estimation with industrial case studies (section 4).

276 The variogram characterization, required to estimate the degree of a spatial  
 277 correlation among points, is a fast procedure. The procedure only takes one single  
 278 measurement with a single image field of a surface to be measured. It is worth noting  
 279 that from a single image, a total of  $\sim$  one million points are obtained. A single image is

280 sufficient to characterize the variogram because in an empirical variogram estimate  
 281 every couple of points counts as a variance estimate replica.

282 The flatness of the three materials was calibrated by means of a traceable CMM with  
 283  $E_{0,MPE}=2+L/300 \mu\text{m}$ . Methods selected for the calibration are multi-position and multi-  
 284 measurement strategies. A total of four different positions for the part were considered  
 285 during the calibration of the plates. For each position, five measurements were repeated.  
 286 By this method, an uncertainty contribution of the volumetric error of the CMM is also  
 287 taken into account in the total calibration uncertainty. The results of the flatness  
 288 calibration and their uncertainty are (notation is based on GUM [4]): aluminum =  
 289  $25.1(8) \mu\text{m}$ , stainless steel =  $4.8(1) \mu\text{m}$ , and titanium =  $4.1(2) \mu\text{m}$ .

290 To yield the data on which to define the variogram models, the plates were measured  
 291 having the optical axis of the FVM approximately perpendicular to the plate itself, using  
 292 the scan parameters in Table 1. The empirical variogram was then evaluated on these  
 293 scanned surfaces. The variogram models in Eq. 4 are least-square fitted and the  
 294 parameters  $s$ ,  $n$ , and  $r$  are calculated. The model is selected based on the highest  $R^2$   
 295 value of the data fitting. Table 2 presents the selected variogram models and their  $R^2$   
 296 value for the considered three materials (Al, SS, Ti). Detailed variogram  
 297 characterizations can be found in [17]. The nugget effect has been indicated equal to 0  
 298 because its value did not differ significantly from 0. This indicates a very strong  
 299 statistical correlation among measurement errors at short distances, which is due to the  
 300 FVM measurement principle based on a focus value calculated over a small patch of  
 301 pixels.

302 Regarding the vertical and lateral resolution, they are set following the default values  
 303 proposed by the instrument manufacturer with a  $5\times$  objective lens. It is worth noting  
 304 that the selected lateral resolution is larger than the pixel size of the instrument. For the  
 305  $5\times$  objective lens, the pixel size is  $1.76 \mu\text{m}$ . But, the actual resolution (the smallest  
 306 distance between two features that can be resolved) will be larger than the pixel size  
 307 due to the working principle of the instrument. As the measuring principle of the  
 308 instrument needs the consideration of a patch of pixels around the considered point to  
 309 calculate the focus measure that defines the  $z$ -level of the point, the effective resolution  
 310 is reduced by the averaging effect of the focus measure estimated on the patch (see  
 311 figure 3).

312 **Table 1** Measurement parameter for Al, SS, and Ti materials.

Material	Exposure time [ $\mu\text{s}$ ]	Contrast	Vertical Resolution [ $\mu\text{m}$ ]	Lateral Resolution [ $\mu\text{m}$ ]
Aluminum	114.4	1.33	0.4	7.82
Stainless steel	116.4	1	0.4	7.82
Titanium	224	1	0.4	7.82

313  
 314 **Table 2** Selected variogram model for Al, SS and Ti.

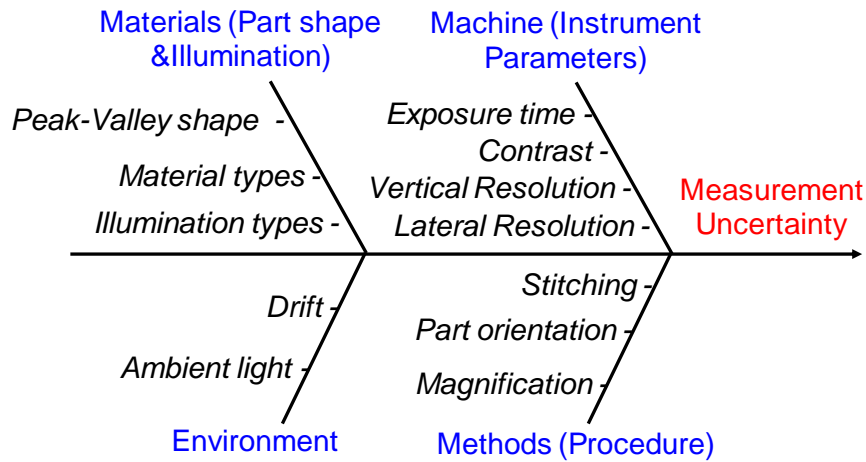
Material	Variogram model	$R^2$	$s$ [ $\mu\text{m}$ ]	$n$ [ $\mu\text{m}$ ]	$r$ [ $\mu\text{m}$ ]
Aluminum (Al)	Exponential	0.56	31	0	114
Stainless steel (SS)	Exponential	0.78	2.8	0	56
Titanium (Ti)	Gaussian	0.71	3.9	0	18

315  
 316 *3.2. Estimation of the contributors to the sill value for the simulation*

317 An extensive experimental campaign was carried out to estimate the various  $s_i$  terms  
 318 involved in FVM measurements. Therefore, the physical aspects of a FVM  
 319 measurement, considered as uncertainty sources, are included into the simulation.



320 A FVM uses a sensor to take a series of images at different distances from a surface.  
 321 A focus value is then calculated and a height is associate to each pixel. In case, stitching  
 322 can be applied to increase the size of the scan. This process is prone to a lot of  
 323 uncertainty sources that cannot be considered by the experiment proposed in section  
 324 3.1. Therefore, more uncertainty sources are estimated. Figure 4 schematically depicts  
 325 the main uncertainty contributors in FVM measurements.  
 326



327  
 328 Figure 4: Diagram of the uncertainty contributors in FVM measurements [17].  
 329

330 An extensive experimental campaign has been conducted to study and quantify the  
 331 effect of the mentioned factors and to include them into the simulation parameters. The  
 332 three materials already mentioned were considered: aluminum (Al, specular surface),  
 333 stainless steel (SS, lambertian surface), and titanium (Ti, lambertian surface). The  
 334 numbers of points produced by a FVM measurement ranges from ~1 to ~4 million 3D  
 335 spatial points. The analysis of variance (ANOVA) has been used to determine the  
 336 significance of the factors.

337 Outliers were removed from the obtained datasets before measurement results could  
 338 be extracted. This procedure is important since a large data point set is obtained from a  
 339 single measurement cycle and outlying points among these points (points presenting a  
 340 very large algebraic deviation compared to other points in the scan) could reduce the  
 341 accuracy of the measurement result. A simple outliers removal procedure has been  
 342 applied, i.e. points having a deviation greater than  $3\sigma$  from the fitting plane or cylinder  
 343 of data points (depending on measured form) were removed, where  $\sigma$  is the sample  
 344 standard deviation of all point deviations (residuals), that are distances from points to  
 345 the fitted geometry.

346 A Shapiro-Wilk test, applied to the residuals (errors) of measured points, proved  
 347 normality of the deviations with  $p$ -value around 0.8 for all the datasets. Figure 5 shows  
 348 the histogram of the deviations (residuals) of points to the fitted plane for the three  
 349 materials. The red line is the fitted Gaussian density function. The standard deviation  
 350 ( $\sigma$ ) of the residuals is presented in Table 3.

351 In this uncertainty characterization studies, the standard deviation  $\sigma$  of measurement  
 352 residuals due to different parameters and measurement conditions is considered as  
 353 parameter characterizing the impact or effect on the measurement uncertainty. The  
 354 measurement residuals are  $\sigma$  of point deviations (a point distance error) to a fitted  
 355 geometry, e.g. a plane, sphere and cylinder.  
 356

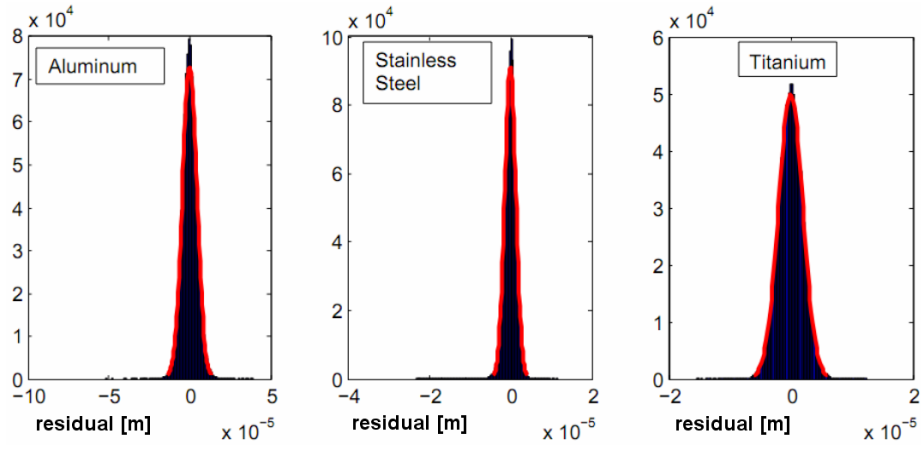


Figure 5: Histogram of residual from a fitted plane for the Aluminum, Stainless steel and Titanium materials.

**Table 3** Standard deviation of residuals for the three materials.

Material	$\sigma$ [ $\mu\text{m}$ ]
Aluminum (Al)	4.49
Stainless steel (SS)	1.37
Titanium (Ti)	2.00

3.2.1 Influence of ambient light and different magnification lenses

A randomly structured surface of a polymeric injection-molded part was used to evaluate this contribution. The polymeric surface is considered because it has a high surface diffusivity and low roughness < 200 nm. Therefore, the surface is smooth and good to estimate the measurement repeatability in the study and to understand the effect of ambient light in a FVM measurement.

Measurements were carried out at 5 $\times$  and 10 $\times$  magnifications, both with the ambient light switched on or off. Numbers of 20 repetitions were carried out with around ~1 million points in each measurement repetition. Figure 6a plots the sigma of the residuals obtained by measuring with different lens types and ambient illuminations. In this figure, there are two sections. The left section presents results obtained using the 5 $\times$  lens in an illuminated or dark room, while the right section presents the result obtained using the 10 $\times$  lens. The main effect and interaction plot between the objective lenses and ambient light are shown in figure 6b and 6c, respectively.

From the obtained results, it seems that no influence of the ambient light is present. The different magnification is significant instead. The  $\sigma$  of the residuals at 10 $\times$  reduces to 2.8  $\mu\text{m}$  from the 3.7  $\mu\text{m}$  obtained at 5 $\times$ . The interaction between magnifications and ambient light is found to be not statistically significant. The range of  $\sigma$  for the lighted and dark room is around 0.01  $\mu\text{m}$ . Meanwhile for difference lenses (magnification factor), the range is around 1.3  $\mu\text{m}$ .

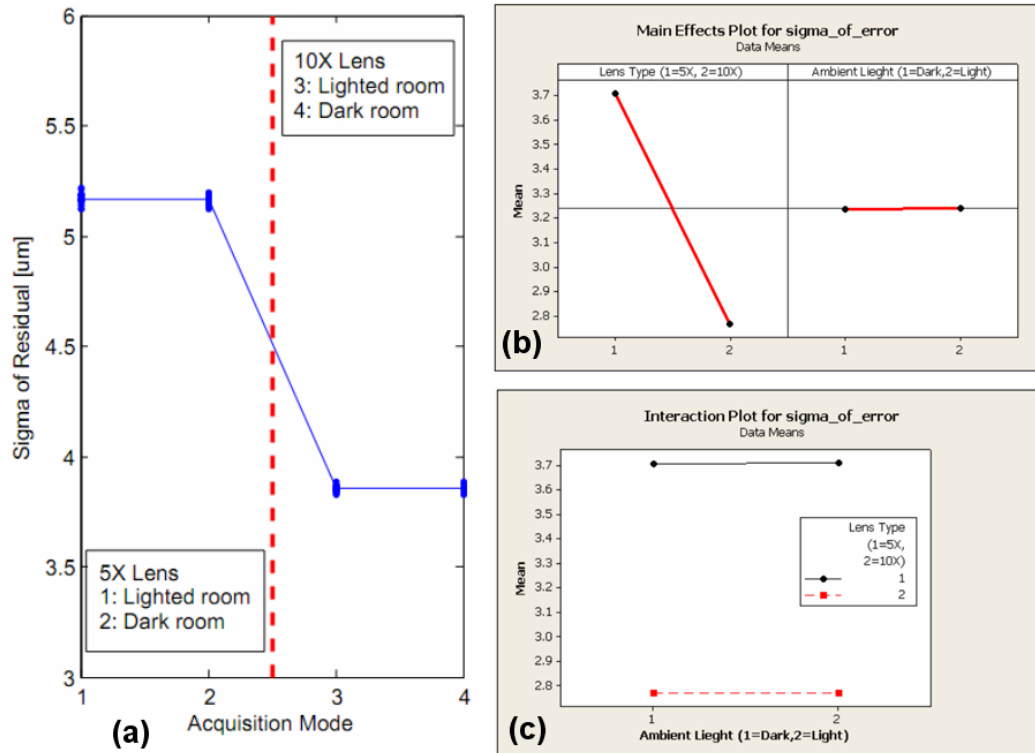


Figure 6: (a) Plot of sigma of residual obtained by different lenses and ambient light, (b) Main effect and (c) Interaction plot between the two factors.

### 3.2.2 Influence of different types of illumination

In this study, two materials were used, aluminum (specular) and random-structured polymer (lambertian) [18]. A 5× magnification was used. For each sample, 20 measurements were carried out (~1 million points each). The FVM instrument is equipped with three illuminators: axial-light, ring-light and polarized-light. From the analysis, different illuminations significantly affect  $\sigma$ .

From figure 7, for the aluminum surface (specular) the difference of  $\sigma$  from ring-light to polarized light reduces by about 0.6 μm, while for the polymer one, it increases by about 0.45 μm. Furthermore, the  $\sigma$  has inverse behavior when moving from specular to lambertian surface. Note that the plot of  $\sigma$  for the lambertian surface is only for ring light and polarized light since the surface cannot be captured with the axial light. The range of  $\sigma$  the different types of illumination with lambert surface is around 0.5 μm and with specular surface is around 1 μm.

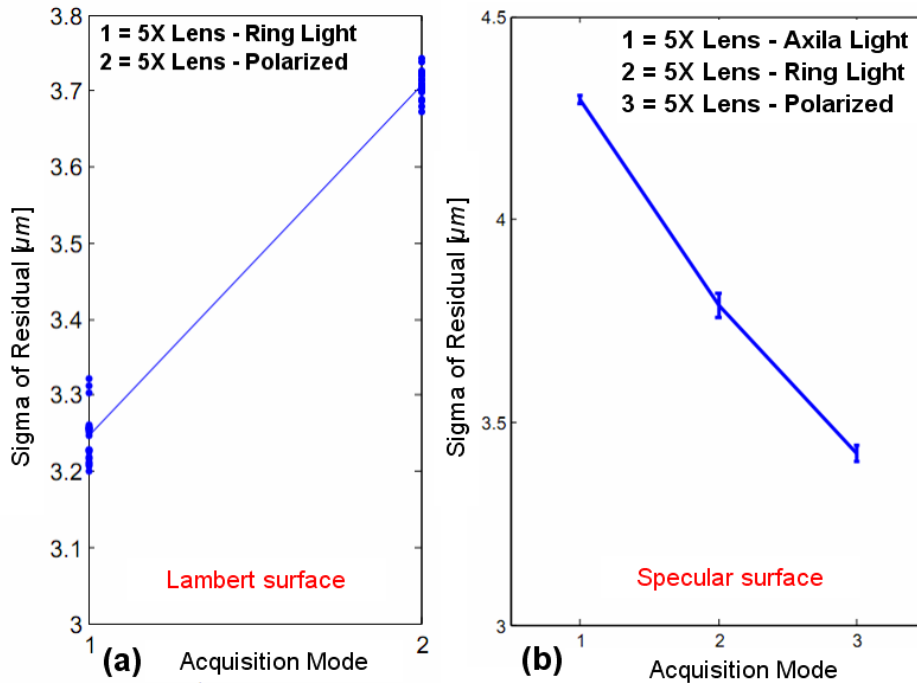


Figure 7: Effect of different illuminations for (a) Lambert surface and (b) Specular surface.

### 3.2.3 Influence of part orientations (surface slopes)

The three flat samples made respectively of aluminum, stainless steel, and titanium with the addition of coated steel (lambertian) and steel (specular) were used. The measurements were carried out for four different positions and steepness/slope orientations ( $0^{\circ}$ ,  $5^{\circ}$ ,  $10^{\circ}$ ,  $15^{\circ}$ ). There are four position types which are combinations of two types of sample placement directions (along  $x$ -axis/horizontal or along  $y$ -axis/vertical) and two types of rotation directions (clockwise or anti-clockwise). Five measurement repetitions were carried out using the  $5\times$  objective lens, so in total 80 measurements were carried out for each material.

From the analysis, it is found that these factors significantly affect the  $\sigma$ . The range of  $\sigma$  for different types of measurement for aluminum, stainless steel and titanium varies around  $2.5\ \mu\text{m}$ ,  $2\ \mu\text{m}$  and  $1\ \mu\text{m}$ , respectively. Figure 8 shows the plot of  $\sigma$  for each experiment as well as the measurement process (position and tilt/orientation direction). Figure 8 shows the plot of  $\sigma$  for different positions and different degrees of steepness (orientation). Note that for steel there are no data when the steepness is higher than  $5^{\circ}$  due to the specular reflectivity of the steel material, which causes the measurement to fail. The range of  $\sigma$  for the part orientation is around  $3\ \mu\text{m}$  considering the highest range value observed is for aluminum-ring light (figure 8 right: blue line).

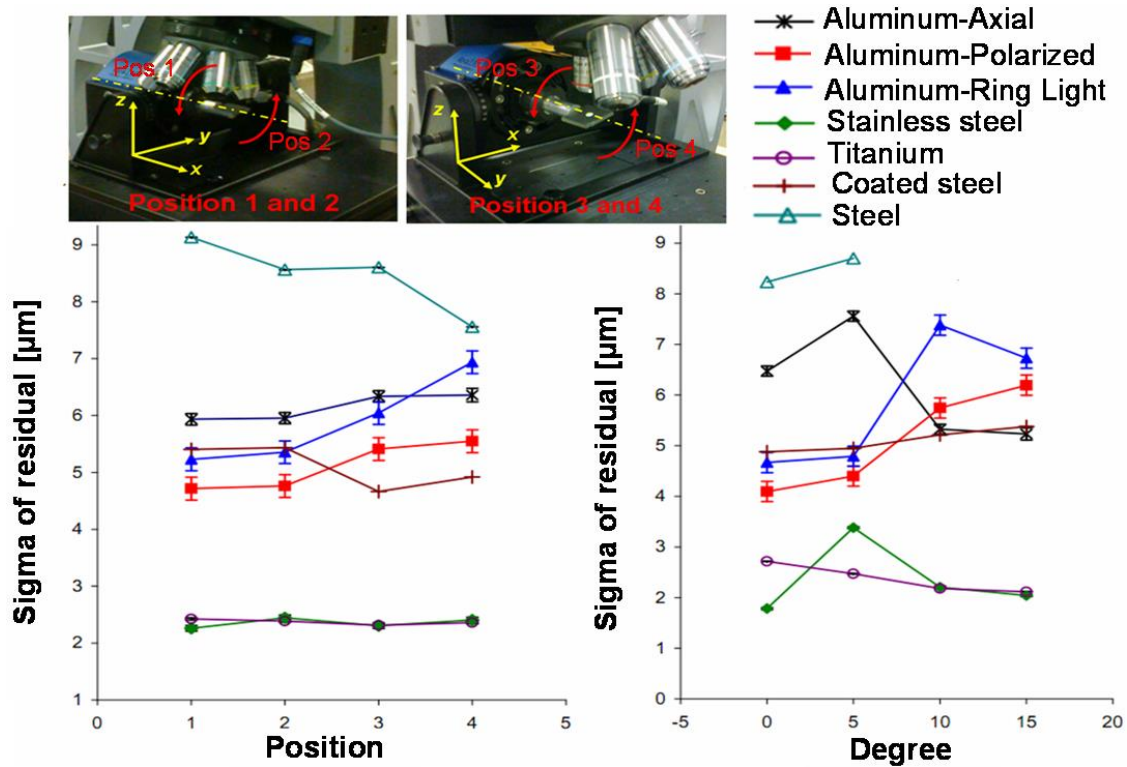
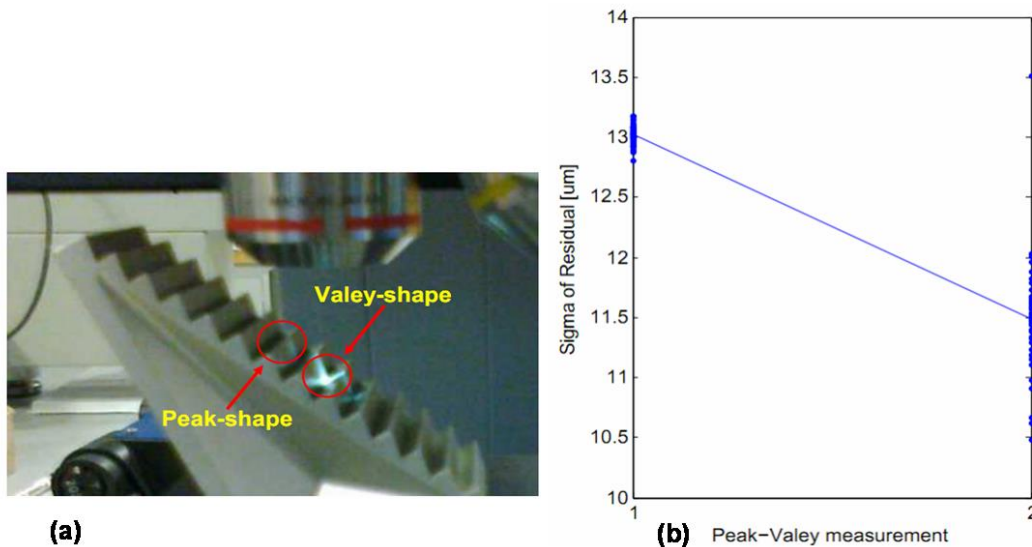


Figure 8: Results of  $\sigma$  for part orientation experiments.

428  
429  
430  
431  
432  
433  
434  
435  
436  
437  
438  
439  
440  
441

### 3.2.4 Influence of peak-valley shape measurements

A machined part having peak and valley features (saw-tooth), made of glazed aluminum with grey color (lambertian), has been used. The edge of the machined part (either peak or valley) was measured 50 times. Each measurement generated about 45000 points. The  $\sigma$  in this case is the standard deviation of the distance of a point to a fitted 3D line representing an edge feature. The results show a statistically significant difference of  $\sigma$  between the two different shapes. The  $\sigma$  of peak measurement is lower by about 1.5  $\mu\text{m}$  with respect to the valley one. The peak-valley measurement and the obtained  $\sigma$  are shown in figure 9. The range of  $\sigma$  for the peak-valley shape contributor is around 2.2  $\mu\text{m}$  (by neglecting some outliers points in figure 9).



442  
443

Figure 9: (a) Peak-valley measurement and (b) Obtained  $\sigma$  of residual.

444 3.2.5 *Stitching/no-stitching measurements*

445

446 Two types of sphere measurement were carried out: a single image (no-stitching) and  
447 four multiple images measurements. The measured part is an ISO 3290-1 steel sphere  
448 [19]. Numbers of 50 measurement repetitions were carried out generating ~750000  
449 points per scan for a single image measurements and ~ 3250000 points for multiple  
450 ones. Table 4 provides details of the results of a point repeatability. The point is derived  
451 from the center of a fitted sphere to the obtained points.

452 The results show that the  $\sigma$ , in  $x$ -,  $y$ - and  $z$ -direction, of measurements by stitching are  
453 two times lower than the one without stitching. Hence, by stitching procedure, there is  
454 an averaging effect to the calculated position of the obtained points which suppresses  
455 part of the random error. Form errors in table 4 are the minimum distance between two  
456 concentric spheres covering all the obtained points. The range of  $\sigma$  for the stitching of  
457 multiple image measurements is around 0.9  $\mu\text{m}$ .

458

459

**Table 4:** Repeatability of a single point.

Measurement type	Form Error / $\mu\text{m}$	
	Mean	Sigma ( $\sigma$ )
Single image	13.27	2.39
Multiple images	13.5	1.45

460

461 3.2.6 *Influence of measurement parameters*

462

463 There are four main parameters of an FVM measurement: exposure time, contrast,  
464 vertical and lateral resolutions. These factors can be controlled by the user before the  
465 measurement is carried out. A flat sample made of titanium was used for the study.  
466 There are four considered levels for lateral and vertical resolution factors and three  
467 levels for exposure time and contrast factors. The range of the lateral and vertical  
468 resolutions is based on the resolution limit of a 5 $\times$  objective lens used for the  
469 experiments. Conversely, the selected range for exposure time and contrast were based  
470 on the range in which a good scan of the surface can be obtained. Table 5 and Table 6  
471 present details of the lateral-vertical study and brightness-exposure time study,  
472 respectively.

473 From the analysis of experiment for the lateral and vertical resolution factors, it is  
474 found that only the lateral resolution is significant. As it can be seen in figure 10, the  
475 lower the lateral resolution is, the smaller the  $\sigma$  is. Decimation of points for bigger  
476 lateral resolution could be the reason for the reduction of noise since there is an  
477 averaging effect in data processing algorithms. There is no interaction effect between  
478 lateral and vertical resolutions as it can be observed in figure 11.

479 These results can be applied in practice for geometric measurement, in particular form  
480 measurement. As stated by Evans [11] optical instruments have considerably larger  
481 noise compared to contact ones. As form measurement is very sensitive to noise a larger  
482 lateral resolution is preferable to suppress measurement noise. The range of  $\sigma$  for the  
483 lateral and vertical resolution are around 3  $\mu\text{m}$  and 0.01  $\mu\text{m}$ .

484

485

486

487

488

**Table 5:** Detail of lateral and vertical resolutions influence study.

Type	Level	Resolution	Lateral point distance [ $\mu\text{m}$ ]	Number of obtained points	Replication
Lateral	1	Highest	1.75	~2000000	25
Lateral	2	Medium (default)	2.62	~1000000	25
Lateral	3	Medium to low	4.66	~300000	25
Lateral	4	Lowest	7.82	~100000	25
Vertical	1	Highest	2.62	~1000000	25
Vertical	2	Medium (default)	2.62	~1000000	25
Vertical	3	Medium to low	2.62	~1000000	25
Vertical	4	Lowest	2.62	~1000000	25

489

490

**Table 6:** Detail of brightness and contrast resolution influence study.

Type	Level	Classification	Value set	Lateral point distance [ $\mu\text{m}$ ]	Number of obtained points	Replication
Exposure time	1	Highest	339 $\mu\text{s}$	1.75	~1000000	25
Exposure time	2	Medium (default)	240 $\mu\text{s}$	2.62	~1000000	25
Exposure time	4	Lowest	110 $\mu\text{s}$	7.82	~1000000	25
Contrast	1	Highest	1.5	2.62	~1000000	25
Contrast	2	Medium (default)	1	2.62	~1000000	25
Contrast	4	Lowest	0.5	2.62	~1000000	25

491

492

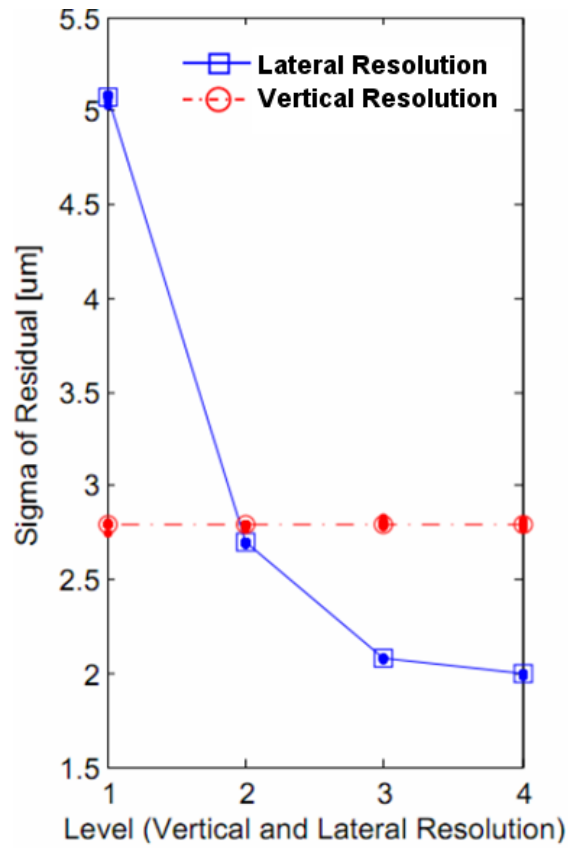


Figure 10: Effect of lateral and vertical resolutions.

493  
494  
495

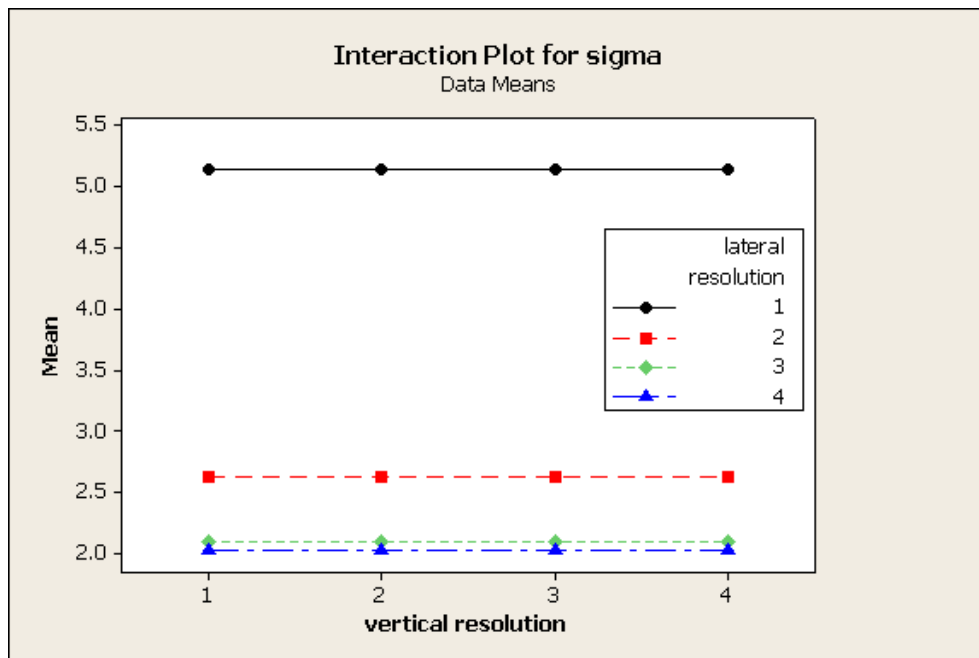


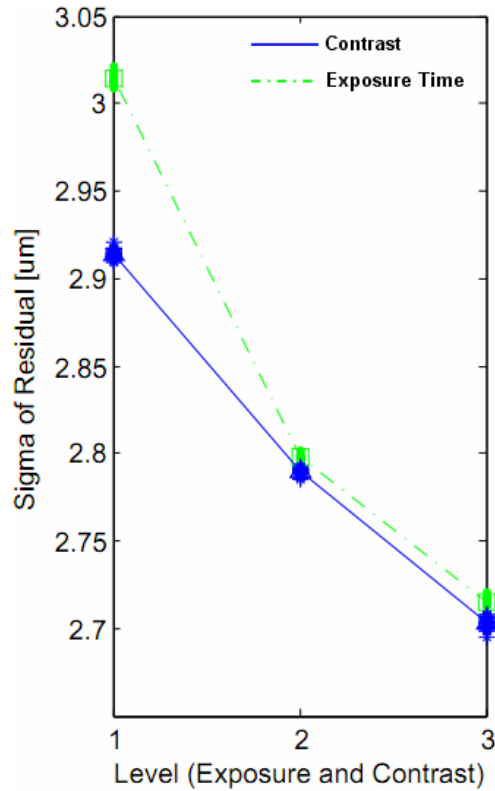
Figure 11: Interaction plot between lateral and vertical resolutions.

496  
497  
498  
499  
500  
501  
502

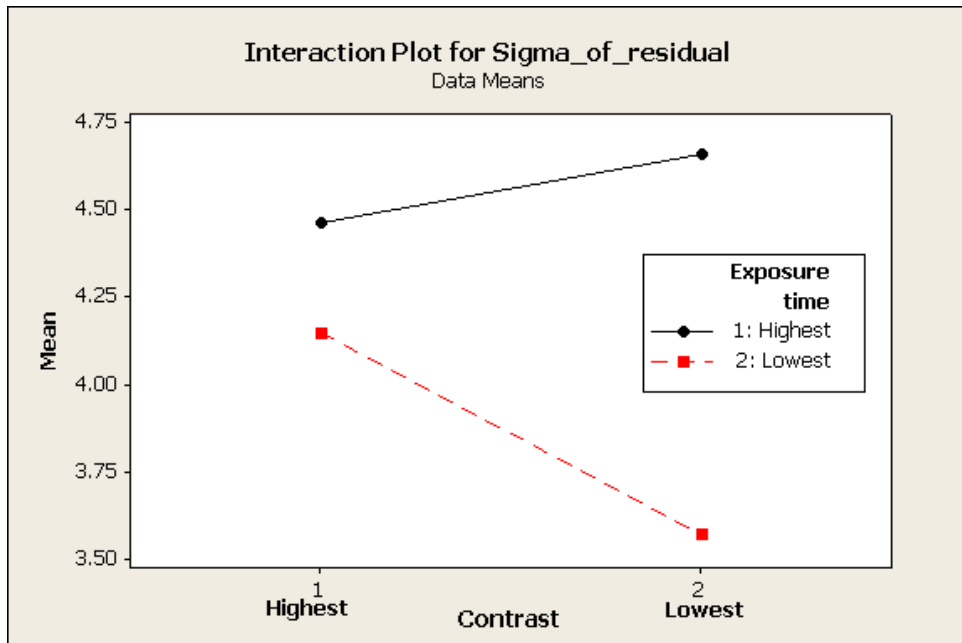
Exposure time (brightness) and contrast effects were then considered. From this analysis, it is shown that exposure time and contrast are significantly affecting the sigma of residual  $\sigma$ . Figure 12 shows that  $\sigma$  decreases when both exposure time and contrast are set to lower values. Interaction between exposure time and contrast is also



503 found significant (figure 13). The range of  $\sigma$  for the contrast and exposure time settings  
 504 are 0.2  $\mu\text{m}$  and 0.3  $\mu\text{m}$ , respectively.  
 505



506  
 507 Figure 12: Effect of different levels of exposure time and contrast.  
 508



509  
 510 Figure 13: Interaction plot between the exposure time and contrast.  
 511

512 3.2.7 Long measurement (drift) behaviors

513  
 514 The variation of  $\sigma$  due to long measurement, both with and without stitching, has been  
 515 investigated. Measurement time was considered because the FVM instrument

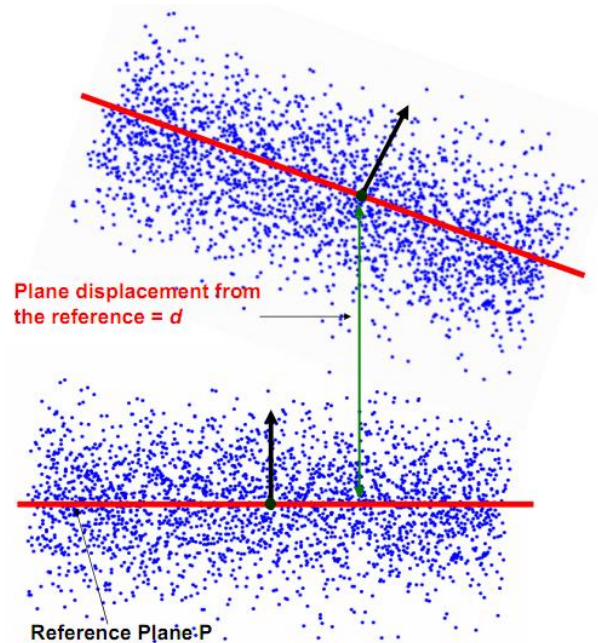
516 components drift can be a relevant uncertainty source. The titanium flat sample has been  
517 used for measurements without stitching.

518 Measurements without stitching do not involve stage movements. Instead, for  
519 measurements with stitching from four images, an ISO 3290-1 steel sphere was used.  
520 The purpose of this type of measurements is to observe the behavior of the instrument  
521 in continuous measurement involving stage movements. Both types of measurements  
522 were carried out continuously without operator interventions. Thanks to a scripting  
523 ability of the instrument, this continuous measurement can be automatically run by the  
524 FVM instrument. The measurement used a 5× magnification lens with default lateral  
525 and vertical resolutions.

526 For non-stitching measurements, a total of 30 runs (~1 million points obtained for  
527 each measurement run) were carried out with a time span of around five hours. Sigma  
528 of residual  $\sigma$  and flatness are calculated for each measurement. Range of  $\sigma$  for this  
529 period of time is 0.0067  $\mu\text{m}$ . Results of flatness measurements show a decreasing trend  
530 up to the 10<sup>th</sup> measurement sequence. The flatness interval (95%) for the first 100  
531 minutes of measurement is 1.25  $\mu\text{m}$ . After this 100 minutes period, the interval becomes  
532 0.62  $\mu\text{m}$ .

533 To represent a systematic error, measurements of distances from  $i$ -th plane to a  
534 reference plane (plane fitted from the first measurement) were conducted as can be seen  
535 from figure 14. In this figure, the systematic error representation is defined as the  
536 distance from the center point of the fitted plane of measurement  $i$  to the reference plane  
537 (plane fitted from the points of the first measurement). They show that the variation  
538 range (95%) of the distance during the first 19 measurements (the first 190 min.) is 0.16  
539  $\mu\text{m}$ , while after this period, it increases to 2.72  $\mu\text{m}$ . Note that the value is shifted one  
540 position to the left, since the 1<sup>st</sup> measurement is not included. Starting from the 20<sup>th</sup>  
541 measurement, juggling phenomena of the measured distance to the reference plane of  
542 the flatness can be observed. These results are presented in figure 15.

543

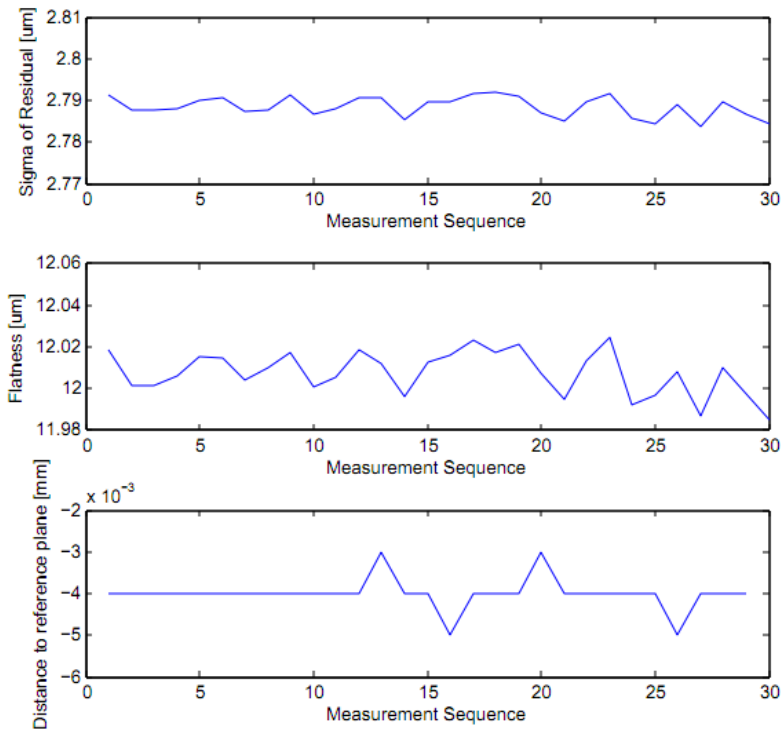


544

Figure 14: Illustration of distance to reference plane.

545

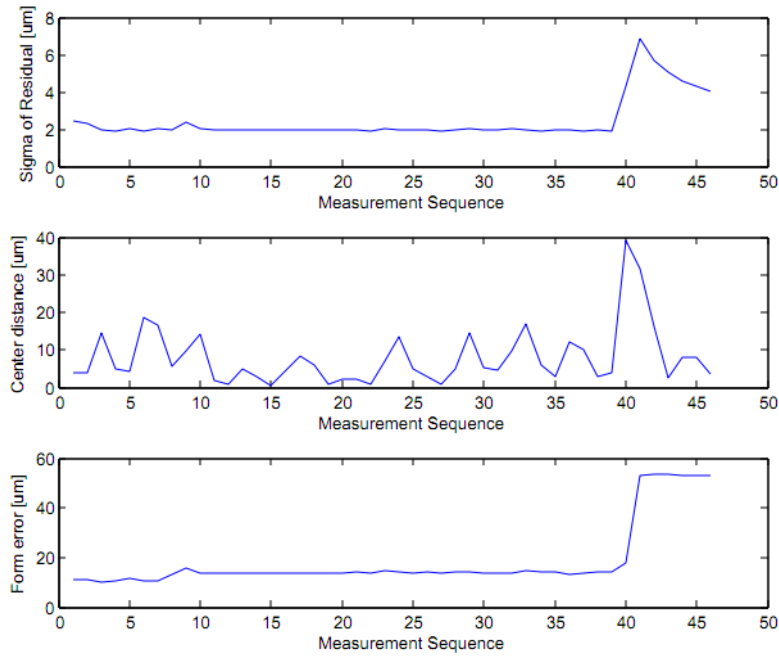
546



547  
 548  
 549  
 550  
 551  
 552  
 553  
 554  
 555  
 556  
 557  
 558  
 559  
 560  
 561  
 562

Figure 15: Long continuous measurement behaviors by plane measurements (without stitching).

Measurements of a sphere with stitching were carried out for 45 runs (~3 millions of points for each measurement run) which correspond to a six hour period. Parameters calculated from the measurement include sigma of the residuals  $\sigma$ , the distance of two consecutive centers and the sphere form error. The sigma of the residuals is used to represent a random error. For a systematic error representation, distances between two consecutive centers are calculated. A stable variation was observed during the first 40 measurements (the first 320 minutes). A shifting is observed for  $\sigma$  after 320 minutes is around 3  $\mu\text{m}$  and for form error is about 40  $\mu\text{m}$ , while the shift between the center distances is about 25  $\mu\text{m}$ . Figure 16 presents the plot of the measurement drift behavior for this type of measurement. The range of  $\sigma$  for the drift is around 2  $\mu\text{m}$ .



563  
564  
565  
566  
567  
568  
569  
570  
571  
572  
573  
574

Figure 16: Long continuous measurement behavior by sphere measurements (with stitching).

### 3.3 Summary of the contributions

Finally, to summarize all the results from the uncertainty characterisation study, table 7 shows the range of the variation of  $\sigma$  for all the considered factors (worst-case scenarios). These values, that are considered relevant in each measurement task, are the  $s_i$  values included in the sill  $s_{sim}$  parameter used in the simulation model (equation 5).

**Table 7:** Summary of the influence of the factors.

Factor	Effect	$\sigma$ [ $\mu\text{m}$ ]
Peak-Valley shape	Significant	2.2
Illumination type with lambert surface	Significant	0.5
Illumination type with specular surface	Significant	1
Lateral Resolution	Significant	3
Vertical Resolution	Not Significant	0.01
Exposure time	Significant	0.3
Contrast	Significant	0.2
Stitching	Significant	0.9
Magnification	Significant	1.3
Part orientation	Significant	3
Drift	Significant	2
Ambient light	Not Significant	0.01

## 575 4. Validation

576 The ISO/TS 15530-4 standard [10] is the basis for the application and validation to  
577 guarantee the traceability of a simulation-based uncertainty estimation in coordinate  
578 metrology. As there are several deeply different coordinate measuring systems, the  
579 ISO/TS 15530-4 standard cannot define a general methodology for simulating the  
580 measurement and stating the uncertainty based on the simulation results. Instead, the  
581 ISO/TS 15530-4 standard defines the general requirements for the simulation, and the  
582 procedures for validating the uncertainty statements, thus guaranteeing the traceability.

583 The validation according to the ISO/TS 15530-4 standard includes both the  
584 mathematical model and the model parameters. The ISO/TS 15530-4 states that:

585

586 “Performing a number of measurements on calibrated objects, the coverage of the  
587 uncertainty ranges is checked. The plausibility criterion should be satisfied for an  
588 appropriate percentage of the time (95% for  $k = 2$ ); this criterion is that a statement of  
589 uncertainty is plausible if:  $|y - y_{cal}| / \sqrt{U_{cal}^2 + U^2} \leq 1$ ”.

590

591 In this method, one should then calculate a  $E_n$  value for each measurement run.  $E_n$  is  
592 formulated as:

593

$$594 \quad E_n = |y - y_{cal}| / \sqrt{U_{cal}^2 + U^2} \quad (9)$$

595

596 where  $y$  is a measurement result,  $y_{cal}$  is the calibrated value of  $y$ ,  $U_{cal}$  is the expanded  
597 calibration uncertainty, and  $U$  is the expanded uncertainty obtained by simulation. If  
598 the expansion factor  $k$  is equal to 2, a good agreement can be concluded if  
599 approximately 95% of total measurements runs are characterized by  $E_n < 1$ .

600 Several case studies of geometric measurements are considered to validate the  
601 proposed simulation method; they include form (flatness measurements) and size  
602 measurements (diameter and height measurements). More complicated case studies can  
603 be found in [17]. It is worth to note that although the components are not a micro-sized  
604 component, the portion of features of the measured component and tolerances are at  
605 micro-scale [1, 2]. In the case study, the variogram model, used for uncertainty  
606 estimations by the proposed simulation, are selected based on the type of the material  
607 of the cased study considered.

608

#### 609 4.1 Flatness measurement

610

611 The three calibrated samples originally adopted for the definition of the variogram  
612 models were considered (see §3.1). The simulation is applied to points obtained from a  
613 real measurement. Therefore, feature form deviation of the part is already included [20].  
614 Figure 17 qualitatively shows that a variogram based simulation yields better results  
615 compared to a simulation of uncorrelated points. The red line shows the simulation  
616 result if the variogram model is applied: it is clear that it is close to the original data.  
617 Instead, if the noise is simulated as pure white noise with a standard deviation equal to  
618 the sill  $s$  of the variogram, the simulation result is far from the original data (green  
619 points).

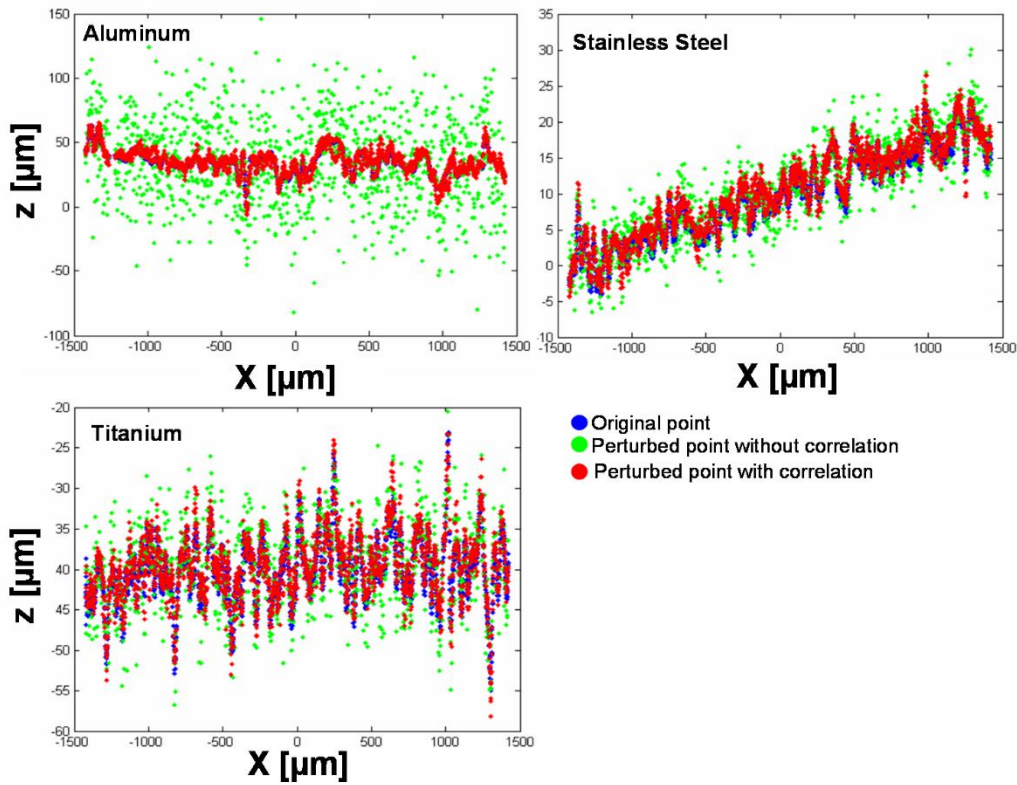
620 Numbers of 100 flatness measurement runs were carried out by changing the part  
621 orientation (approximately perpendicular to the optical axis,  $5^\circ$  tilted clockwise and  
622 anticlockwise) to represent an orientation error when placing the part. The measurement  
623 parameters used followed those shown in Table 1 for each material type and orientation.  
624 To evaluate the uncertainty, 500 simulation runs were carried out. The sill  $s$  parameter  
625 of the simulation was modified according to Eq. (5) to consider the influence of the  
626 various uncertainty factors in the real measurement situation of the flatness  
627 measurement. Figure 18a shows results of the flatness measurements. It is worth noting  
628 that the flatness is based on a min-max fitting. This kind of fitting in general generates  
629 a non-Gaussian distribution of the measurement results.

630

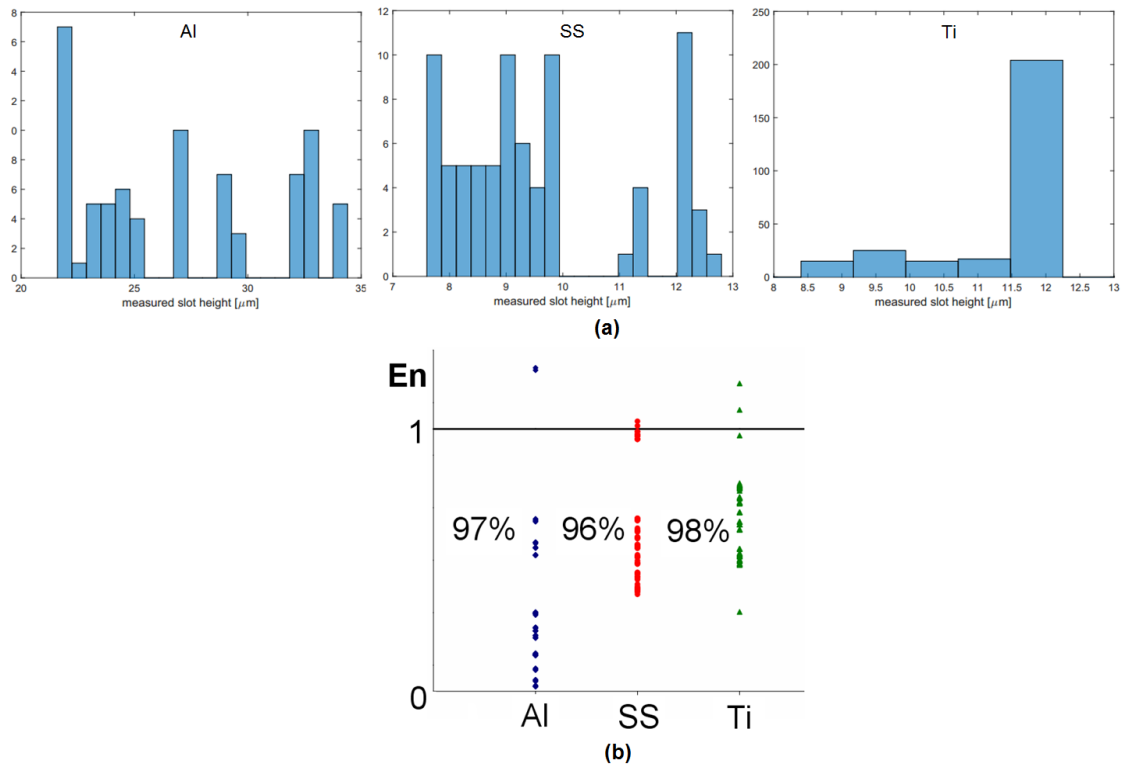
631 The flatness samples were calibrated on a traceable tactile-CMM with  $E_{0;MPE} = 2 +$   
 632  $L/300 \mu\text{m}$  where  $L$  is the measured length in mm (the CMM is periodically performance  
 633 verified). The calibrations follows a multiple-measurements strategy that vary the  
 634 position and orientation of the samples during the calibration process to take into  
 635 account the volumetric error of the traceable tactile-CMM. Calibration results of the  
 636 flat samples are  $y_{\text{cal}} = 25.1 \mu\text{m}$  and  $U_{\text{cal}} = 1.6 \mu\text{m}$  for Al,  $y_{\text{cal}} = 4.8 \mu\text{m}$  and  $U_{\text{cal}} = 0.2$   
 637  $\mu\text{m}$  for SS, and  $y_{\text{cal}} = 4.1 \mu\text{m}$  and  $U_{\text{cal}} = 0.4 \mu\text{m}$  for Ti.

638 The estimated  $U$  for Al, SS, and Ti are  $14.0 \mu\text{m}$ ,  $7.7 \mu\text{m}$ , and  $10.1 \mu\text{m}$ , respectively.  
 639 From calculation of each  $E_n$  value, the fraction of  $E_n$  values for which  $E_n < 1$  for Al, SS,  
 640 and Ti are 97%, 96%, and 98% respectively (Figure 18b), so the simulator can be  
 641 considered validated in this case. From figure 18, some portions of  $E_n$  are larger than  
 642 one. Having some portion of  $E_n > 1$  suggest that the estimated uncertainty by the  
 643 proposed simulation is not overestimating the expected uncertainty. Similar explanation  
 644 for the  $E_n$  values are valid for all other presented case studies in this paper.

645  
 646



647  
 648 Figure 17: Plot of original points (blue) superimposed with the simulated points  
 649 without considering (green) and with considering (red) the correlation among points  
 650 for aluminum (Al), stainless steel (SS), and titanium (Ti).  
 651

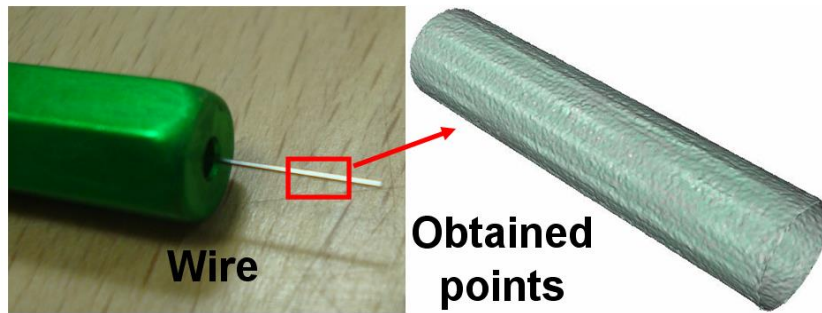


652  
 653 Figure 18: Plot of (a) histogram of the flatness value and (b)  $E_n$  values for the flatness  
 654 measurement of Al, SS, and Ti.  
 655

#### 656 4.2. Commercial micro-wire measurements

657 The measurement of a diameter (a dimensional characteristic) is presented in this  
 658 case. An industrial micro steel wire with diameter of  $310 \pm 2 \mu\text{m}$  was measured (Figure  
 659 19). The wire is used as a plug-gage to measure the nozzle diameter of a water jet  
 660 machine. Since the part is a commercial plug-gage,  $y_{\text{cal}}$  and  $U_{\text{cal}}$  are based on the part's  
 661 nominal specifications. The  $y_{\text{cal}}$  is considered to be equal to  $310 \mu\text{m}$ . The  $U_{\text{cal}}$  of the  
 662 plug-gage diameter is estimated as a type B uncertainty and is assumed to have a  
 663 rectangular distribution. Hence,  $U_{\text{cal}}$  is equal to  $2.31 \mu\text{m}$ .

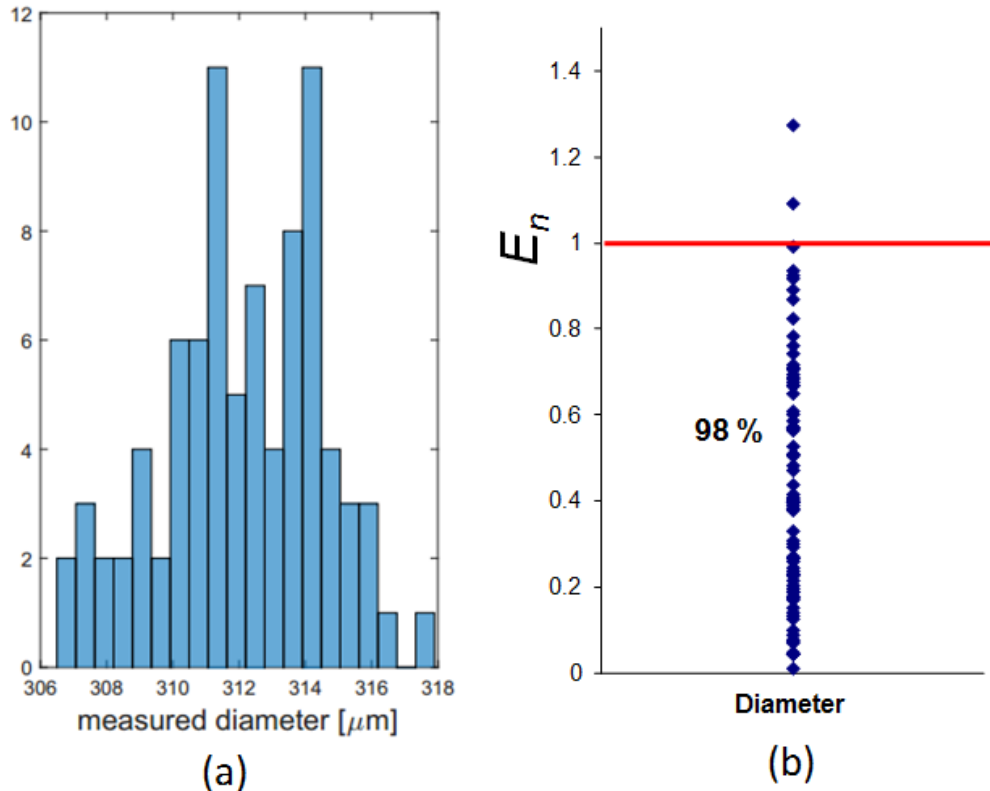
664 Before running the simulation, the procedure, explained in Section 2, to determine  
 665 the variogram model was carried out for steel since the variogram model of the steel  
 666 material used in this case study has not yet been determined. The selected variogram  
 667 model is a Gaussian one with  $s$ ,  $n$ , and  $r$  parameters equal to  $34.4 \mu\text{m}$ ,  $0 \mu\text{m}$ , and  $14.8$   
 668  $\mu\text{m}$  respectively. The estimated  $U$  is  $5.6 \mu\text{m}$  obtained from 500 simulation runs  $y$ . A  
 669 total of 85 measurement runs  $y$  were carried out with the following measurement  
 670 parameters: 193.2 ms (exposure time), 0.44 (contrast),  $0.6 \mu\text{m}$  (vertical res.) and  $3.9$   
 671  $\mu\text{m}$  (lateral res.) by using  $10\times$  objective lens. From the  $E_n$  calculation, a total of 98 %  
 672 values have  $E_n < 1$ , thus ensuring validation. The histogram of the measurement results  
 673  $y$  and the  $E_n$  calculation for each measurement are shown in figure 20. In figure 20  
 674 right, around 2 % of  $E_n$  values are more than one.  
 675



Specification: dia.  $310 \pm 2 \mu\text{m}$

Figure 19: The micro-wire.

676  
677



678  
679  
680  
681

Figure 20: (a) Histogram of the diameter measurement results and (b)  $E_n$  values for the diameter measurement validation.

682  
683

#### 4.3. Step-height measurements of a slot-milled steel component

684  
685  
686  
687  
688  
689

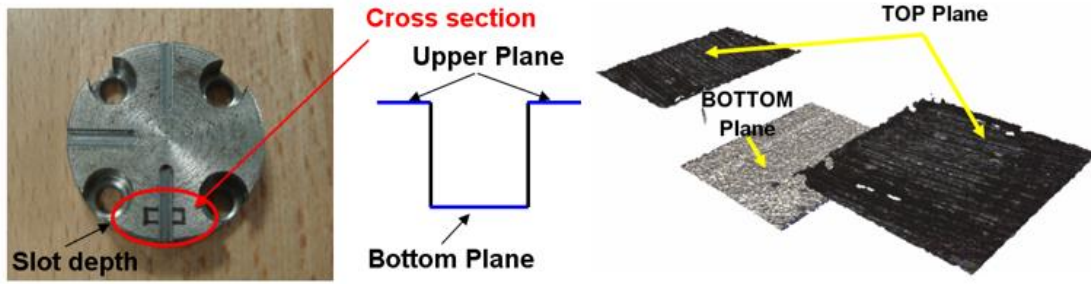
A measurement of the step-height of a slot-milled part is presented in this study. The part was made of a steel material by using a precision micro-milling machine. The part, the slot height definition and an example of the measured surface are shown in figure 21. Measurement parameters for the slot step-height measurement are exposure time =  $88.32 \mu\text{s}$ , contrast = 0.2, lateral resolution =  $7.83 \mu\text{m}$  and vertical resolution =  $0.4 \mu\text{m}$  by using a  $5\times$  objective lens.

690  
691  
692  
693  
694  
695

The results of a calibration process using a traceable tactile-CMM are  $y_{\text{cal}} = 698.7 \mu\text{m}$  and expanded uncertainty  $U_{\text{cal}} = 0.25 \mu\text{m}$ . Total of 100 measurements runs  $y$  was carried out. From around 500 simulations runs to estimate the uncertainty of the slot measurement, an expanded estimated uncertainty  $U$  is obtained as  $0.45 \mu\text{m}$ . From a total of 100 measurement runs  $y$ , 93% (almost 95%) of  $E_n$  values are less than 1, hence the simulation and the uncertainty estimation are validated. Figure 22 shows the



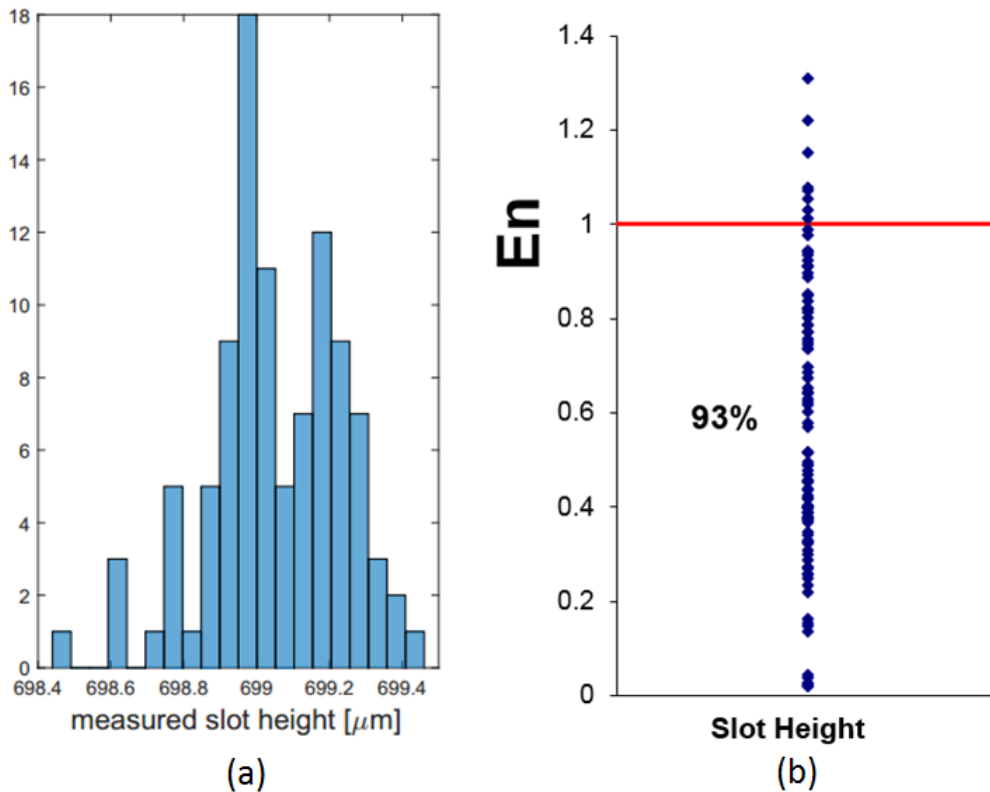
696 histogram of the measurement results and the  $E_n$  value calculation for each  
 697 measurement.  
 698



The measured slot      The measured surface

Figure 21: The measured slot and its obtained surface.

699  
 700  
 701



702  
 703  
 704

Figure 22: (a) Histogram of the height measurement results and (b)  $E_n$  values for the slot step-height measurement validation.

705 **5. Conclusions**

706 This paper presents a proposal of a simulation-based approach to estimate the task-  
 707 specific measurement uncertainty of a 3DM performing geometric inspections. A case  
 708 study regarding FVM is proposed. The case study is validated according to the ISO/TS  
 709 15530-4 standard. The method considers the correlation among points obtained by the  
 710 optical instrument since correlation naturally occurs among points measured  
 711 sequentially or continuously. Variogram models are determined for each material to  
 712 represent the property of correlations among points. In general, the correct type of  
 713 variogram (Gaussian, exponential, spherical, etc.) is defined based on the gathered  
 714 experimental data. In this work, we are suggesting and describing a possible approach

715 we developed and validated in a case study. The proposed approach can be applied to  
716 other type of 3DM instruments and can be implemented and integrated into instruments  
717 software system as a module.

718 Extensive uncertainty characterization has been carried out to identify and quantify  
719 the uncertainty sources and incorporate them into the simulation parameters. The  
720 validation is carried out with industrial case studies and the results show that the  
721 simulated uncertainties have a good agreement with the real measurement.

722 The proposed simulation approached can be summarised as follows:

- 723 1. Define the variogram model and quantify the  $s$ ,  $n$  and  $r$  parameters for each  
724 material type. This step is carried out once for every different material.
- 725 2. Experimentally evaluate the additional uncertainty sources not considered in the  
726 variogram, but influencing the measurement result. The uncertainty sources  
727 quantification is carried out once for each type of instrument.
- 728 3. Measure the part to inspect, and compute the measured value  $y$ .
- 729 4. Having modified the value of  $s$  considering the additional sources of uncertainty,  
730 apply the variogram model to generate an adequate number of simulation runs  
731 and the related perturbed clouds of points, compute the simulated measured values  
732 and, based on these values, estimate the expanded uncertainty  $U$ .
- 733 5. State the measurement result  $y \pm U$ .

734 Further works include building a database of optimal variograms for various types of  
735 materials and applying the proposed method to estimate task-specific uncertainty for  
736 surface texture measurements.

737

### 738 **Acknowledgements**

739

740 Financial support to this work has been provided as part of the project REMS - Rete  
741 Lombarda di Eccellenza per la Meccanica Strumentale e Laboratorio Estesio, funded by  
742 Lombardy Region (Italy), CUP: D81J10000220005 and AMala – Advanced  
743 Manufacturing Laboratory, funded by Politecnico di Milano (Italy), CUP:  
744 D46D13000540005.

745 Acknowledgment is due to the Recruitment Program of High-end Foreign Experts of  
746 the Chinese State Administration of Foreign Experts Affairs.

747

### 748 **References**

- 749 [1] L. Alting, F. Kimura, H. Hansen, G. Bissacco, *Micro engineering, CIRP Annals*  
750 *- Manufacturing Technology* 52 (2) (2003) 635–657. doi:10.1016/S0007-  
751 8506(07)60208-X.
- 752 [2] H. Hansen, K. Carneiro, H. Haitjema, L. De Chiffre, *Dimensional micro and*  
753 *nano metrology, CIRP Annals - Manufacturing Technology* 55 (2) (2006) 721–743.  
754 doi:10.1016/j.cirp.2006.10.005.
- 755 [3] ISO/IEC, *ISO/IEC GUIDE 99:2007(E/F): International vocabulary of*  
756 *metrology - basic and general concepts and associated terms (VIM) (2007).*
- 757 [4] G. Moroni, S. Petrò, W. Syam, *Four-axis micro measuring systems*  
758 *performance verification, CIRP Annals - Manufacturing Technology* 63 (1) (2014)  
759 485–488. doi:10.1016/j.cirp.2014.03.033.
- 760 [5] G. Moroni, W. Syam, S. Petrò, *Performance verification of a 4-axis focus*  
761 *variation co-ordinate measuring system, IEEE Transactions on Instrumentation and*  
762 *Measurement* 66 (1) (2017) 113–121. doi:10.1109/TIM.2016.2614753.
- 763 [6] ISO/IEC, *ISO/IEC GUIDE 98-3: Uncertainty of measurement - Part 3: Guide*  
764 *to the expression of uncertainty in measurement (GUM:1995) (2008).*

765 [7] R. Wilhelm, R. Hocken, H. Schwenke, Task specific uncertainty in coordinate  
766 measurement, *CIRP Annals - Manufacturing Technology* 50 (2) (2001) 553–563.  
767 doi:10.1016/S0007-8506(07)62995-3.

768 [8] G. Moroni, S. Petrò, Optimal inspection strategy planning for geometric  
769 tolerance verification, *Precision Engineering* 38 (1) (2014) 71–81.  
770 doi:10.1016/j.precisioneng.2013.07.006.

771 [9] International Organization for Standardization, ISO 15530-3: Geometrical  
772 Product Specifications (GPS) – Coordinate measuring machines (CMM): Technique  
773 for determining the uncertainty of measurement – Part 3: Use of calibrated workpieces  
774 or standards (2011).

775 [10] International Organization for Standardization, ISO/TS 15530-4: Geometrical  
776 Product Specifications (GPS) - Coordinate measuring machines (CMM): Technique for  
777 determining the uncertainty of measurement - Part 4: Evaluating task-specific  
778 measurement uncertainty using simulation - First Edition (Jun. 2008).

779 [11] C. Evans, Uncertainty evaluation for measurements of peak-to-valley surface  
780 form errors, *CIRP Annals - Manufacturing Technology* 57 (1) (2008) 509–512.  
781 doi:10.1016/j.cirp.2008.03.084.

782 [12] J.-P. Kruth, N. Van Gestel, P. Bleys, F. Welkenhuyzen, Uncertainty  
783 determination for cmms by monte carlo simulation integrating feature form deviations,  
784 *CIRP Annals - Manufacturing Technology* 58 (1) (2009) 463–466.  
785 doi:10.1016/j.cirp.2009.03.028.

786 [13] C. Cheung, M. Ren, L. Kong, D. Whitehouse, Modelling and analysis of  
787 uncertainty in the form characterization of ultra-precision freeform surfaces on  
788 coordinate measuring machines, *CIRP Annals - Manufacturing Technology* 63 (1)  
789 (2014) 481–484. doi:10.1016/j.cirp.2014.03.032.

790 [14] E. Trapet, F. Waeldele, The virtual CMM concept, in: P. Ciarlini, M. Cox,  
791 F. Pavese, D. Richter (Eds.), *Advanced Mathematical Tools, II*, World Conference  
792 Scientific, Singapore, 1996, pp. 238–247.

793 [15] R. Leach (Ed.), *Optical Measurement of Surface Topography*, Springer-Verlag,  
794 Berlin, Germany, 2011. doi:10.1007/978-3-642-12012-1.

795 [16] N. A. C. Cressie, *Statistics for Spatial Data*, 1st Edition, Wiley-Interscience,  
796 New York, 1993.

797 [17] W. P. Syam, [www.politesi.polimi.it/handle/10589/100382](http://www.politesi.polimi.it/handle/10589/100382)Uncertainty  
798 evaluation and performance verification of a 3d geometric focus variation  
799 measurement, Ph.D. thesis, Politecnico di Milano, Milan, Italy (2015).  
800 [www.politesi.polimi.it/handle/10589/100382](http://www.politesi.polimi.it/handle/10589/100382)

801 [18] D. A. Forsyth, J. Ponce,  
802 <https://books.google.it/books?id=gM63QQAACAAJ>Computer Vision: A Modern  
803 Approach, Always learning, Pearson, 2012. <https://books.google.it/->  
804 [books?id=gM63QQAACAAJ](https://books.google.it/books?id=gM63QQAACAAJ)

805 [19] International Organization for Standardization, ISO 3290-1: Rolling bearings –  
806 Balls – Part 1: Steel balls (2014).

807 [20] J. M. Baldwin, K. D. Summerhays, D. A. Campbell, R. P. Henke, Application  
808 of simulation software to coordinate measurement uncertainty evaluations, *NCSLI*  
809 *Measure* 2 (4) (2007) 40–52. doi:10.1080/19315775.2007.11721398.

810